MOLECULAR CANCER BIOLOGY

INTERNATIONAL JOURNAL of CANCER

Distinct invasive patterns in situ between estrogen receptor-positive and triple-negative breast cancer through the intraductal tracking of carbon nanoparticles

Xinwen Kuang[1,2,3] | Zixuan Luo[1] | Zhihong Sun[1,4] | Jiawei Hu[1] | Jianhua Liu[1] | Deguang Kong[1] | Guannan Wang[5] | Liantao Guo[1] | Lan Luo[1,6] | Weijie Zheng[1] | Shengrong Sun[1] | Yan Rao[7] | Chuang Chen[1]

[1]Department of Breast and Thyroid Surgery, Renmin Hospital of Wuhan University, Wuhan, People's Republic of China

[2]Peking Union Medical College, Chinese Academy of Medical Sciences, Peking Union Medical College Hospital, Beijing, People's Republic of China

[3]Department of Plastic Surgery, Peking Union Medical College Hospital, Beijing, People's Republic of China

[4]Department of Burn and Plastic Surgery, Shandong Provincial Hospital Affiliated to Shandong First Medical University, Jinan, People's Republic of China

[5]Lombardi Comprehensive Cancer Center, Georgetown University, Washington, DC, USA

[6]Department of Breast Surgery, The Affiliated Hospital of Guizhou Medical University, Guiyang, People's Republic of China

[7]Animal Biosafety Level III Laboratory at the Center for Animal Experiment, Wuhan University School of Basic Medical Sciences, Wuhan, People's Republic of China

Correspondence
Chuang Chen, Department of Breast and Thyroid Surgery, Renmin Hospital of Wuhan University, No 238 Jiefang Road, Wuchang District, Wuhan, Hubei 430060, People's Republic of China.
Email: chenc2469@whu.edu.cn

Yan Rao, Animal Biosafety Level III Laboratory at the Center for Animal Experiment, Wuhan University School of Basic Medical Sciences, Wuhan, Hubei 430000, People's Republic of China.
Email: rao@whu.edu.cn

Abstract

Given that the transition from ductal carcinoma in situ (DCIS) to invasive breast cancer (BC) is crucial during the BC progression, the mechanism involved in the invasion transition behind triple-negative breast cancer (TNBC) and estrogen receptor-positive (ER-positive) subtype has remained elusive. This article detected distinct invasion patterns of BC cells between the ER-positive and TNBC using intraductal murine models with intraductal administration of carbon nanoparticles (CNPs). First, the feasibility of the utility of CNPs as a tracer was proved. The area ratio of CNPs and tumor cells invading the stroma at the late stage was found significantly higher than that in the early stage in MNU-induced ER-positive BC. However, opposite results were obtained in the triple-negative model. Consequently, we proposed that the ER-positive phenotype cells behave differently between different stages during tumor progression while there is no such difference in the invasion process of TNBC cells. The analysis regarding the duct integrity along with immunohistochemical characteristics further explained the distinct invasion features between the ER-positive and triple-negative subtypes. Last, the relationship between the duct thickness and the duct integrity suggested that ER-positive tumors gradually increased in size within the lumen before the invasion. Overall, this study suggested the different invasion characteristics of ER-positive BC and TNBC in vivo.

What's new?

Compared to triple-negative breast cancer, estrogen receptor-positive breast cancer presents a lower risk of metastatic disease. The specific mechanisms behind the distinct prognoses remain to be explored. Here, the authors tracked the invasion of breast cancer cells in vivo models using intraductal injection of carbon nanoparticles as a minimally invasive technique. The results suggested that estrogen receptor-positive breast cancer cells invade and migrate within the duct until the tumor is large enough to break through the duct lining in the late phase, while triple-negative tumor cells begin the migration and invasion in the early stage.

1 | INTRODUCTION

Breast cancer (BC) which grows to be one of the most common cancers as well as the leading cause of death among women worldwide, is highly heterogeneous.[1-4] Molecular classification of BC based on gene expression subdivides breast tumors into distinct prognostic groups using ER, progesterone receptor (PR) and epidermal growth factor receptor 2 (HER2) status.[5] ER-positive BC with a relatively low proliferative nature and better prognosis express the ER.[6-8] TNBC is a highly metastatic form of breast cancer, accounting for 10% to 20% of all BC.[9,10] This subtype tends to occur distant metastasis in the early stage.[11,12] Previous investigations have been conducted to identify the mechanism that drives the higher invasiveness of TNBC compared to ER-positive or HER2-positive BC. The utility of proteomic analysis comparing the triple-negative tumors and other phenotypes of BC has identified molecular mechanisms which are exclusively activated in the TNBC.[13-17] Similarly, comprehensive genomic profiling has revealed specific gene amplification, which contributes to the invasiveness of TNBC.[18-22]

We combined the ER-positive BC model previously established by our lab and a mouse intraductal (MIND) model representing the TNBC with intraductal administration of specific nanomaterials as a tracer to understand the distinct invasion pattern.[23] Rats administrated with N-methyl-N-nitrosourea (MNU) have been widely used to study breast carcinogenesis due to the ability to replicate the occurrence of human breast cancer.[24-27] In previous work, we developed the rat model by intraductal injection of MNU with a fully predictable tumor location.[23] By gene expression profiles, tumors in this model cluster with the ER-positive subtype of human BC. Likewise, the MIND model based on 4T1 cells has the advantage of presenting disease progression from DCIS to invasive carcinoma compared to the traditional fat pad model.[28-34] In combination, these intraductal models allow us to observe how breast tumor cells migrate and invade.

CNPs are harmless nanomaterials consisting of nanoscale carbon particles with an average particle size of 150 nm.[35-39] Complete removal from the body via a combination of hepatic and renal clearance allows CNPs to be widely used, such as drug and gene delivery, lymph node tracing and biosensors.[40-42] In these two models, CNPs are inoculated intraductally into the rodents to track the motion of tumor cells (Figure 1A,B). This study first demonstrated the feasibility of using CNPs to track cancer cells and revealed the distinct invasive mode between the ER-positive type and TNBC. We verified that ER-positive BC cells invade and migrate until the tumor within the ducts is large enough to break through the duct lining in the late phase. In contrast, triple-negative tumor cells begin the migration and invasion in the early stage (Figure 1B). This is the first study to present and track the invasion of BC cells in vivo models, which helps understand the invasive transition of ER-positive and triple-negative mammary tumors.

2 | MATERIALS AND METHODS

2.1 | Animals

Female Sprague-Dawley (SD) rats aged 3 to 4 weeks and female BALB/c mice (after twice gestation) used in this study were acquired from Hunan Silaike Jingda Laboratory Animal Co, Ltd (Changsha, China). All the animals were maintained in a 12-hours light-dark cycle and acclimated for at least 5 days before the experiments. All the rodents were provided with a standard laboratory diet and distilled water in specific pathogen-free rooms. Animals were euthanized by carbon dioxide inhalation.

2.2 | Cell culture

Luciferase transgenic 4T1 (4T1-Luc, RRID: CVCL_J239) breast cancer cells (Shanghai Yaji Biological Technology, Shanghai, China) were developed with vectors carrying luciferase and puromycin resistance genes. The 4T1-Luc cells and 67NR cells (RRID: CVCL_9723; Shanghai Yaji Biological Technology, Shanghai, China) represent an aggressive phenotype of human triple-negative BC with expression loss of ER, PR and a nonmetastatic phenotype of human ER-positive BC, respectively. Before transplantation, the cells were confirmed mycoplasma-free and then trypsinized, washed through centrifugation, resuspended in phosphate-buffered saline (PBS) and counted by a Bürcker chamber. All experiments were performed with mycoplasma-free cells.
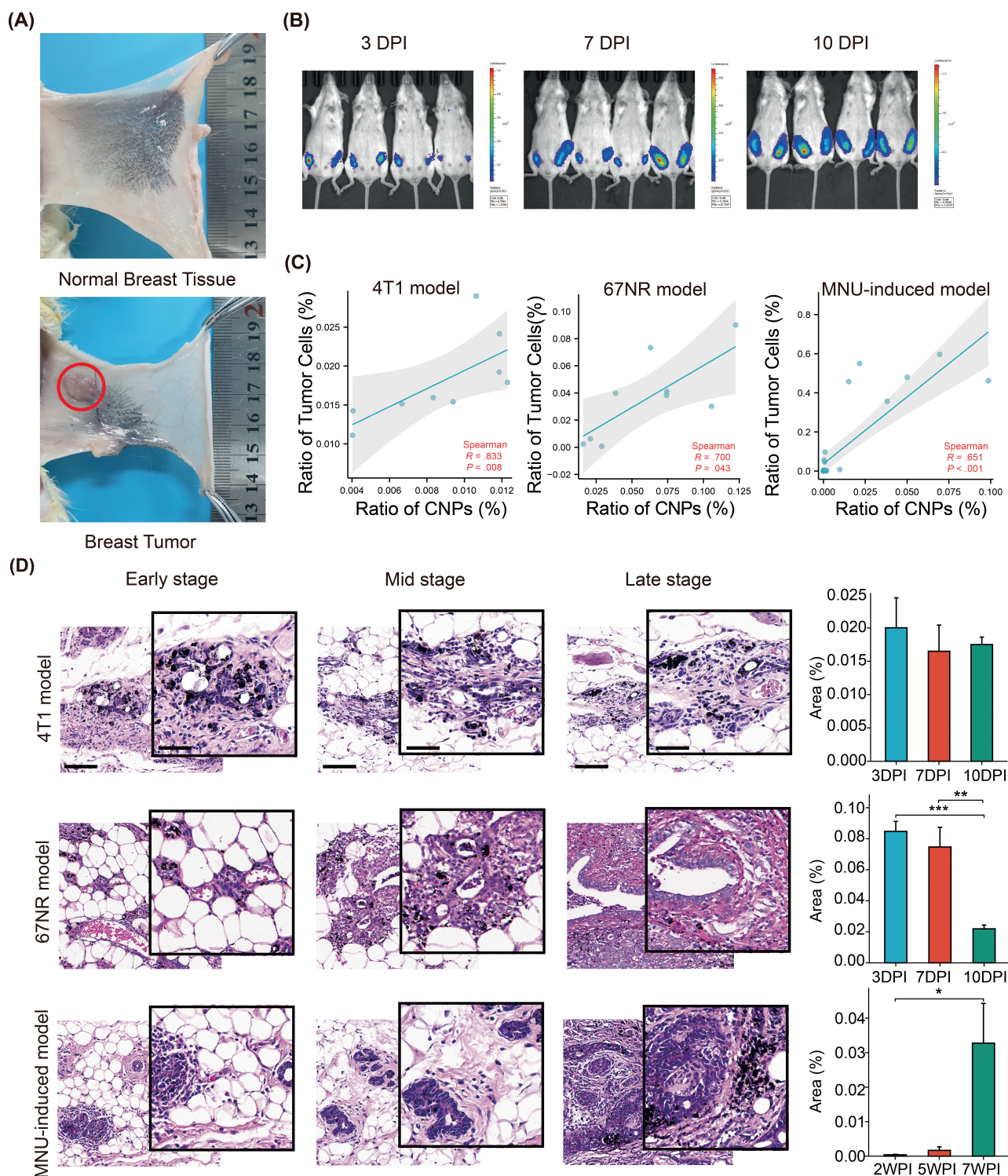
FIGURE 1 The distribution of CNPs tracks the invasion of BC cells of ER-positive and triple-negative subtypes after intraductal administration. (A) The intraductal administration of CNPs suspension in both the normal mammary (Top) and the cancerous breast (Bottom) offered the chance to observe the mammary ducts with the naked eye. The red circle shows the breast tumor. (B) The intraductal route implanted 4T1-Luc cells in female BALB/c mice, and whole-body imaging of BALB/c mice was performed at different times to observe the luciferase-expressing 4T1 cells and ensure the establishment of tumors. (C) Correlation plot of the ratio of the ductal breakthrough CNPs area and cancer cells for the 4T1, 67NR and MNU-induced models. (D) The H&E staining (Left) of the 4T1, 67NR and MNU-induced models exhibited the ductal breakthrough of CNPs. The quantification (Right) of the percentage of the area of CNPs that penetrated the ductal epithelial layer of the total area in the 4T1, 67NR and MNU-induced models. Data are mean ± SD. Statistical analysis was performed using the Kruskal-Wallis test, Spearman correlation and one-way ANOVA when appropriate. Scale bars, 100 μm and 50 μm, respectively. [Color figure can be viewed at wileyonlinelibrary.com]

2.3 | The 4T1 and 67NR MIND model

To establish the 4T1 and 67NR models, female BALB/c mice (after twice gestation) were intraductally injected into the duct opening of the bilateral fourth mammary glands with 20 μL, 2×10^5 BALB/c-derived 4T1-Luc mammary tumor cells or 67NR tumor cells (10^7/mL). The CNPs suspension (0.5 mL: 25 mg; carbon nanoparticles, LUMMY Pharmaceutical Co, Ltd, Chongqing, China) was diluted with normal saline. After the modeling process, the animals were inoculated with a 10-fold dilution of the carbon nanoparticles suspension (CNPs suspension; 5 g/L, 20 μL/teat) at 2, 6 and 9 days postinoculation (DPI), respectively. Of note, the intraductal injection of CNPs suspension allowed us to observe the distribution of the CNPs in the animals. Exactly 24 hours after the injection of CNPs suspension, the mice were sacrificed and dissected to collect tumor tissues. In vivo small animal imaging was conducted before the CNP administration to ensure the successful establishment of 4T1 breast tumors. The inoculation was performed using a 100 μL Hamilton syringe with a 33-gauge blunt needle under anesthesia. The mice were tagged and grouped randomly three to five animals in each group.

2.4 | Intraductal MNU mammary tumor model in rats

Based on our previous study, 3- to 4-week-old female SD rats received intraductal administration of freshly prepared MNU (50 g/L, 20 μL/teat; M325815, TRC Chemicals, Ontario, Canada) once in the bilateral fourth mammary glands. The rodents were sacrificed to collect tissue at 2, 5 and 7 weeks postinoculation (WPI). Exactly 24 hours before the sacrifice, the rats in the experiment group were inoculated intraductally with the 10-fold dilution of the CNPs suspension (5 g/L, 20 μL/teat). During the injection, animals were maintained under anesthesia using continuous 2% isoflurane inhalation (1% oxygen). Carcinoma in situ with positive expression of ER, and negative expression of Her-2 developed 28 to 42 days after the first intraductal injection of MNU and eventually progressed to invasive ductal carcinoma.[23,43] The animals were randomized to three groups of three to five rats each.

2.5 | Histopathology and immunohistochemistry

The rodent mammary tissues were isolated, fixed overnight in phosphate-buffered 10% formalin and embedded in paraffin. Then tissue sections were deparaffinized at 5 μm. Paraffin sections were rehydrated with decreasing ethanol concentrations, inferior to hematoxylin and eosin (H&E) staining. For further analysis, tissue sections were dehydrated and mounted with cover glass. Immunohistochemistry (IHC) was utilized to detect the level of E-cadherin, α-SMA and CD31 in the breast samples. After standard dewaxing and rehydration, tumor samples were incubated in citric acid buffer (pH 6.0) for 15 minutes for antigen retrieval, followed by treatment with 3% H_2O_2 for 10 minutes to inactivate endogenous peroxidase activity. Then, the sections were blocked using 5% goat serum (Beyotime Institute of Biotechnology, Shanghai, China) for 10 minutes and incubated with primary antibody. Next, sections were washed and incubated with secondary antibodies at 37°C for 1 hour. For Masson's staining in breast tumor tissue, the fixed tumor tissue was stained with Masson's trichrome according to standard protocols. H&E, IHC and Masson's staining were imaged with a Pannoramic MIDI system (3DHISTECH, Budapest, Hungary).

For the morphometric assessment, the area of the lesion of CNPs and tumor cells that penetrated the ductal epithelial layer and the total area of the tumor section was measured using the CaseViewer software from 3DHISTECH. For quantifying, three ×20 representatives randomly selected, nonadjacent, nonoverlapping images were taken per sample. The intensity of CD31+ lumens was quantified (n = 3). For E-cadherin, α-SMA and Masson's staining, images were analyzed and quantified by Image-Pro Plus 6 software and ImageJ software. Researchers blinded to experimental data counted and calculated the cell density independently, and their mean values were adopted as a result.

Using a standard immunofluorescence protocol, the expression of the fibroblast marker, Vimentin and matrix metallopeptidase 9 (MMP9) was evaluated. Nuclei were counterstained by DAPI. Tissue sections were processed with primary antibodies at 4°C overnight and secondary antibodies at RT for 1 hour. Specific primary antibody to MMP9 was obtained from Abcam, OH (AF5105, 1:500), to Vimentin from SanYing Biotechnology, Wuhan, China (10366-1-AP, 1:1000), to CD31 from Abcam, OH (ab182981, 1:200), to E-cadherin from Proteintech, Wuhan, China (20874-1-AP, 1:500), to α-SMA from Boster, Wuhan, China (BM0002, 1:200). Images were captured with a Pannoramic MIDI slide scanner (3DHISTECH) and quantified by ImageJ software.

2.6 | Flow cytometry analysis

To obtain single-cell suspensions, 4T1 and 67NR tumors were harvested on day 10 post-tumor inoculation. According to the manufacturer's instructions, single-cell suspensions of tumors were prepared using gentleMACS dissociator and digestive enzyme (Miltenyi Biotec). The immune subsets in breast tumors were analyzed and quantified by flow cytometry and the data were acquired using a CytoFLEX flow cytometer (Beckman Coulter, Fullerton, CA). The following mouse antibodies were used: anti-CD8a (APC, clone 53-6.7, #100711, BioLegend), anti-CD4 (FITC, clone RM4-5, #100510, BioLegend), anti-CD49b (PE, clone DX5, #108907, BioLegend), anti-CD11b (FITC, clone M1/70, #101216, BioLegend), anti-Ly6G (PE, clone 1A8, #127607, BioLegend) and, anti-F4/80 (APC, clone BM8, #123115, BioLegend).

2.7 | Transmission electron microscopy

Transmission electron microscopy (TEM) was utilized to verify the morphology of the breast tumor tissue and CNPs. Breast tissues were dissected, cut into 1 mm^3, and fixed in 2.5% glutaraldehyde in PBS

(0.1 M, pH 7.4). After washing three times with PBS, the tissue sections were fixed in 1% osmic acid for 1 hour. Then the samples were dehydrated using graded alcohol and anhydrous acetone. After being buried with epoxy resin, samples were then kept in an electric oven at 37°C overnight. After embedding, the ultrathin sections (60-70 nm) were cut using an ultramicrotome (Leica EM UC7, Leica, Wetzlar, Germany), coated with celloidin membrane, stained with uranyl acetate and lead citrate and then dried overnight. Last, the sample was observed using a Model HT-7800 transmission electron microscope (HITACHI, Tokyo, Japan).

2.8 | In vivo bioluminescence imaging

To ensure the successful establishment of triple-negative breast tumors, in vivo small animal imaging was conducted before the CNP administration. The mice bearing 4T1-Luc tumors were anesthetized and then injected intraperitoneally with 300 μL D-luciferin potassium salt buffer solution (15 mg/mL, Shanghai Maokang Biotechnology, Shanghai, China). Following the standard instructions, the bioluminescence images were assessed using in vivo imaging system (IVIS) Lumina Series III (Perkin Elmer, Waltham).

2.9 | Statistical analysis

The data were represented as mean ± SE of the mean (SEM). The appropriate statistical analysis was completed with the software R (version 3.6.3). Statistical analysis was performed using nonparametric tests, chi-square tests or ANOVA tests when appropriate. Spearman correlation coefficients were used to assess correlations. Probability values (P) <.05 were considered statistically significant. *P < .05; **P < .01; ***P < .001.

3 | RESULTS

3.1 | The distinct invasion modes between BC cells of ER-positive and triple-negative subtypes are tracked by the distribution of CNPs after intraductal administration

We detected the distribution of CNPs in the mammary ducts after intraductal injection in rodents. This black nanomaterial allowed us to observe the mammary ducts with the naked eye (Figure 1A). The in vivo half-life of CNPs was longer than other nanomaterials such as Fe3O4 nanoparticles and showed stronger color contrast (Figure S1A). Furthermore, CNPs suspension is easy to access and easy to use at a low cost. Hence, we chose CNPs as the tracer to reveal the motion of BC cells of ER-positive and triple-negative subtypes.

To demonstrate the invasion of these two BC subtypes, corresponding animal models were established. As shown in Figure 1B, in vivo imaging validated the invasive primary tumor growth of 4T1

tumor cells. It showed that 4T1 cells spread throughout the mammary gland and surrounding tissues. The quantification of the lesion of CNPs and tumor cells that penetrated the ductal epithelial layer as a proportion of the total area was measured at each time point. The ductal breakthrough CNPs area ratio and that of cancer cells had a strong positive correlation in the MNU-induced tumor samples (Spearman correlation, $r = .651$; $P < .001$; Figure 1C). A similar correlation was observed in the 4T1 samples (Spearman correlation, $r = .833$; $P = .008$; Spearman correlation, $r = .700$; $P = .043$; Figure 1C). These results suggested that CNPs can track the migration and invasion of cancer cells in both ER-positive and TNBC models.

Statistical analysis was performed to explore the invasion of breast tumor cells in these models. Notably, the percentage of the area of both ductal breakthrough CNPs and tumor cells was significantly increased at the late phase than that at the early phase in the MNU-induced model. However, no similar disparities were highlighted in the 4T1 model. At 7 WPI, the ratio of the ductal breakthrough CNPs area was much climbed ($P < .05$) in contrast to it at 2 WPI in the MNU-induced tumors (Figure 1D). Likewise, the percentage of tumor cells penetrating the duct at 7 WPI was statistically higher (Figure S1B) than it was at 5 WPI ($P < .05$). But for TNBC, none of the differences among the tumor cell area at 3 DPI, 7 DPI and 10 DPI were statistically significant (Figure S1B). The opposite results between the MNU-induced and 4T1 tumors led us to the speculation about the distinct invasive pattern in these two subtypes. For TNBC tumors, migration and invasion behavior did not differ significantly between different stages, while for the ER-positive phenotype, invasiveness at the early stage was reduced compared to advanced tumors.

3.2 | The differences in histology and immunohistochemical characteristics between ER-positive and triple-negative BC models may explain their distinct invasive pattern

To figure out the mechanics behind the opposite invasion modes, we evaluated the entire pathological sections of each rat group (2 WPI, 5 WPI and 7 WPI) and mouse group (3 DPI, 7 DPI and 10 DPI). Whether the duct contains CNPs categorized mammary ducts as no distribution of CNPs and distribution of CNPs (Figure 2A). In the MNU-induced tumors, 47.1% of ducts at 2 WPI contained no CNPs, while CNPs were distributed in the rest ducts. At 7 WPI, CNPs were distributed in significantly fewer ducts (41.5%, $P < .001$) compared to the 2 WPI group (Figure 2B). A possible explanation is as follows. The first part of this article revealed that the area ratio of CNPs that broke through the basement membrane at 7 WPI was higher than it was at 2 WPI. Consequently, the amount of CNPs in the lumen at 7 WPI was relatively less. This could explain the observed decrease in ducts with CNP distribution at 7 WPI. As for the 4T1 tumors, statistical tests revealed that at 3 DPI, 489 ducts (38.2%) contained no CNPs while CNPs assembled in the rest, 792 ducts (61.8%). Surprisingly, CNPs were distributed in significantly fewer ducts (Figure 2B) at 7 DPI (26.1%, $P < .001$) and 10 DPI (49.0%, $P < .001$). One possible reason is
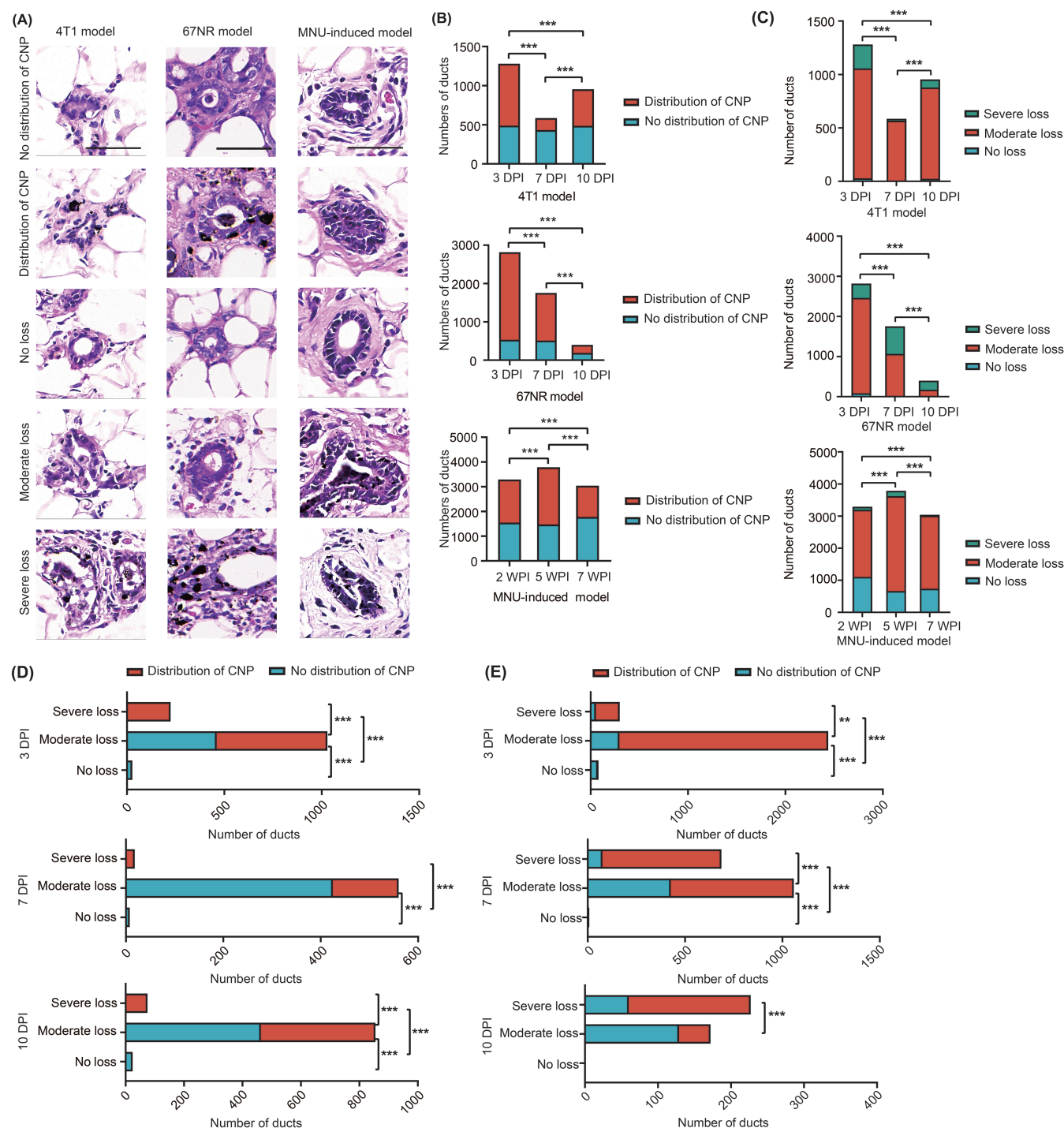
FIGURE 2 The morphological evaluation of pathological sections of each rat group and mouse group. (A) The H&E staining for histological clarification in the 4T1, 67NR and MNU-induced models. (B) The statistical analysis of breast tumors regarding the distribution of CNPs in the ER-positive subtype mammary tumors and for the triple-negative tumors. (C) The histological evaluation and statistical analysis of breast tumors regarding the ductal integrity in the ER-positive subtype mammary tumors and triple-negative tumors. Comparison of the percentage of ducts with CNP distribution in normal, mild defected and severe defected ducts between different stages for the 4T1 (D) and 67NR tumors (E). Data are mean ± SEM. Pearson's χ^2 test was used to compare proportions and evaluate the *P*-value. Scale bars, 50 μm. [Color figure can be viewed at wileyonlinelibrary.com]

that the palpable tumors were established in BALB/c mice before the intraductal administration of CNPs at 6 DPI and 9 DPI. Therefore, CNPs failed to enter the solid tumors by intraductal injection in the 4T1 model.

In the MNU-induced model, segregation according to the integrity of the mammary duct classified 33.5% of ducts of the group at an early stage into normal ducts, 63.6% into ducts with moderate loss of luminal architecture and 2.9% into severe loss group. Compared to

the 2 WPI group, significantly more ducts ($P < .001$) at 5 WPI and 7 WPI in the MNU-induced tumor sections were found with moderate and severe loss of luminal architecture (Figure 2C). The gradual loss of ductal integrity suggested that the invasiveness of MNU-induced tumor cells increases with tumor progression. For the TNBC model, we categorized 28 (2.2%) ducts as normal, 1029 (80.3%) ducts as moderate defected and 224 (17.5%) ducts as severely defected at 3 DPI. Similarly, 8 ducts (1.4%) at 7 DPI and 24 (2.5%) at 10 DPI were classified as normal ducts (Figure 2C). Unlike the MNU-induced tumors, the proportion of the seriously defected ducts at 3 DPI was comparable and even higher than that of the tumors at 7 DPI and 10 DPI. This result indicated that 4T1 cells exhibit strong invasiveness and penetrate the ductal epithelial layer in the early phase. The distinct invasive pattern between the MNU-induced and 4T1 models could be interpreted based on these morphological differences. Furthermore, these findings above coincided with the relatively lower risk of distant metastasis for the ER-positive subtype than TNBC.

Interestingly, differences in the distribution of CNPs within the ducts were observed between groups with varying loss of luminal architecture in both the chemically induced model and grafting models. For the 4T1 model, at 3 DPI, the percentage of ducts with CNP distribution in normal ducts was significantly decreased than in moderate ($P < .001$) and ducts with severe loss of luminal architecture ($P < .001$). The outcomes observed at 7 DPI and at 10 DPI were comparable except that no significant differences ($P = .241$) were found between normal ducts and moderately defected ducts at 7 DPI (Figure 2D). The results for the MNU-induced model (Figure S1C) were similar to the results for the 4T1 model. Together, these results indicated that CNPs followed tumor cells which penetrated the epithelial layer. Therefore, CNPs assembled in ducts with loss of luminal architecture rather than the normal ducts. The findings further explained the correlation between the breakthrough of CNPs and tumor cells and confirmed the validity of CNPs tracing the tumor motion.

To further elucidate the distinction between different stages in-depth, we performed E-cadherin, CD31 and MMP9 staining. Compared to the discontinuous E-cadherin staining at 7 WPI, strong continuous linear membranous retention of E-cadherin was seen at 2 WPI with CNPs limited within the ducts (Figure 3A). Quantitative analysis of E-cadherin staining also confirmed this result (Figure 3B). This further proved the hypothesis that ER-positive tumor cells prefer local proliferation at an early stage, and they penetrate the epithelial layer in late tumors. Furthermore, CD31 staining (Figure 3C,D) demonstrated significantly increased ($P < .05$) CD31+ vessel formation at 7 WPI than at 2 WPI and at 5 WPI in the MNU-induced model. IHC staining of E-cadherin and CD31 in the TNBC model was similar to the principal analysis. Unlike the distinct immunoreactivity for E-cadherin between early-stage and late-stage tumors for ER-positive models, both E-cadherin staining at 3 DPI and 10 DPI in the TNBC subtype was discontinuous and incomplete (Figure 3A). Similarly, quantitative analysis of CD31 staining indicated no significant difference among early, mid and late phases (Figure 3C,D). The opposite results further

demonstrated that the invasion pattern of the ER-positive phenotype is different from that of the triple-negative subtype.

3.3 | The modeling process affected the ductal breakthrough behavior but not the immunohistochemical performance of tumors

We established an intraductal allograft model with an ER-positive breast cancer cell line (67NR) to determine whether the modeling method contributes to the different invasion patterns between the MNU-induced and 4T1 models. First, a strong positive correlation between the ductal breakthrough CNPs area ratio and that of cancer cells in 67NR tumors was proved (Spearman correlation, $r = .700$; $P = .043$; Figure 1C). However, as shown in Figure 1D, the ratio of the ductal breakthrough CNPs area at the early stages of 67NR was significantly higher than at the late stages, which contradicts the MNU-induced model. The result indicated more frequent ductal breakthroughs at early stages in the 67NR model, similar to the 4T1 model. As for the evaluation of CNP distribution, mammary duct integrity and their relationship (Figure 2B,C,E), the results for the 67NR model were also identical to the 4T1 model.

To elucidate the distinction between different stages and different models in-depth, we performed the E-cadherin, α-SMA, CD31 and MMP9 staining for the 67NR model. Interestingly, the immunohistochemical expression pattern change for the 67NR model was similar to the MNU-induced model. Discontinuous staining of E-cadherin and α-SMA was observed in the early and late stages of the 67NR model (Figure 3A,E). However, compared to the early stages, the intensity of E-cadherin and α-SMA was significantly reduced in the late stages for the 67NR model (Figure 3B,F). For CD31 staining, in both the 67NR and the MNU-induced models, a significant increase in microvessel density was observed in the late stages (Figure 3C,D). Oppositely, there were no significant differences between the early-stage and late-stage 4T1 tumors with respect to E-cadherin, α-SMA and CD31 expression (Figure 3B,D,F). These results indicated that the immunohistochemical expression pattern for 67NR is similar to MNU-induced ER-positive tumors. However, 67NR tumor cells exhibited similar ductal breakthrough behavior to the 4T1 model even though the 4T1 model served as metastatic TNBC and 67NR served as nonmetastatic ER-positive breast cancer. This led us to hypothesize that the manner in which 67NR breast tumors are established can greatly impact the biological behavior of tumor cells without affecting their immunohistochemical characteristics. Consequently, the invasive behavior 67NR tumors showed in early stages was similar to that of 4T1 tumors due to the same modeling process.

Researchers found that TNBC has a higher level of tumor-infiltrating lymphocytes (TILs) than other breast cancer subtypes, suggesting a higher degree of immunogenicity.[44,45] It may have a direct correlation with the invasion and metastatic potential of tumors. Therefore, we collected tumors on day 10 after tumor establishment and used flow cytometry to understand the immune cell subset differences between ER-positive and triple-negative breast tumors. Gating
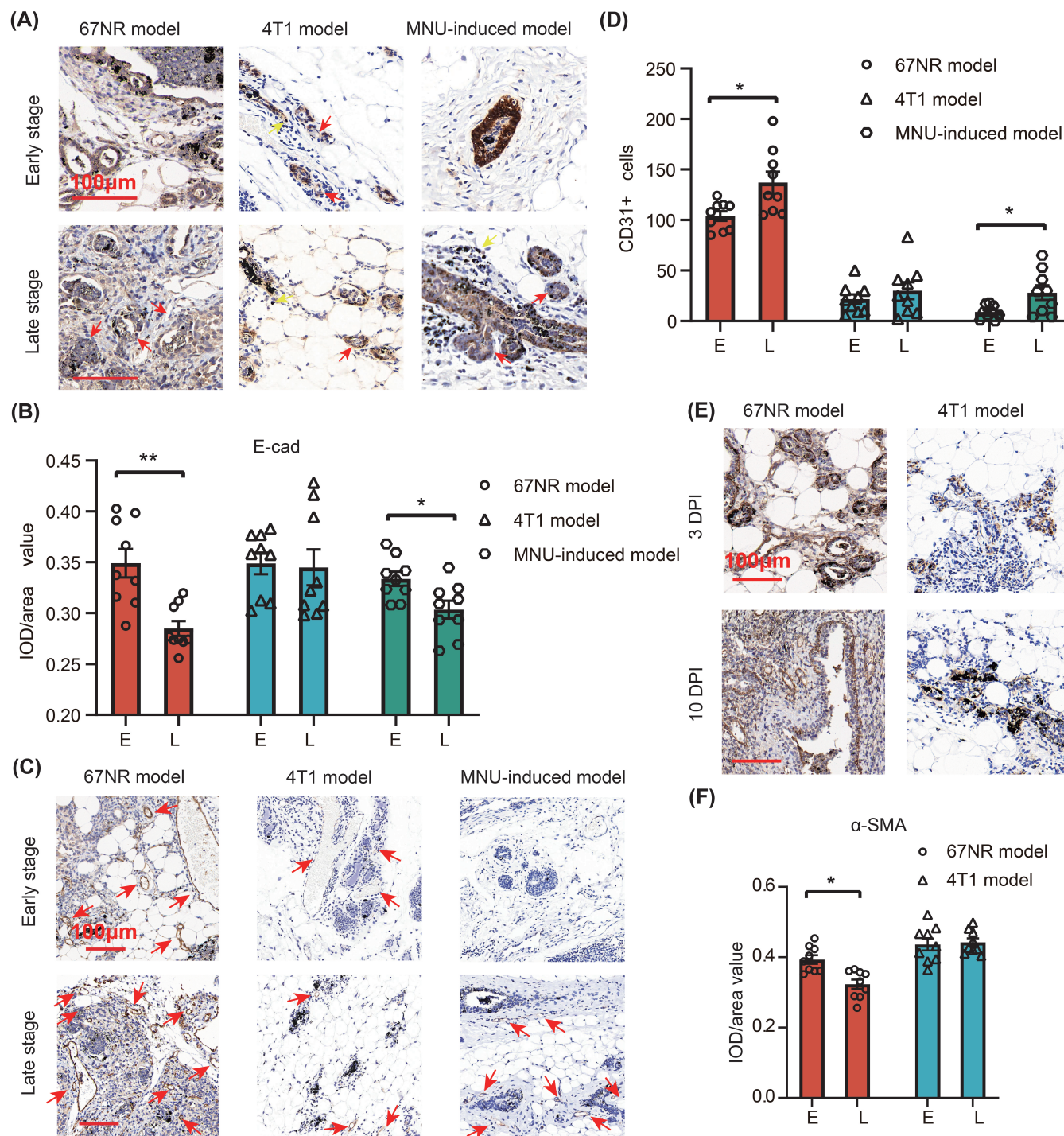
FIGURE 3 The differences in immunohistochemical characteristics between ER-positive and triple-negative BC tumors may explain their distinct invasive pattern. (A) Expression of E-cadherin in the early-stage and late-stage tumors by immunohistochemical staining in the 4T1, 67NR and MNU-induced models. For the MNU-induced ER-positive subtype, red arrows show an interrupted E-cadherin staining, and yellow arrows show CNPs invading the stroma. In the 4T1 model, red arrows show an interrupted E-cadherin staining, and yellow arrows show CNPs invading into the stroma. The pictures of immunohistochemical staining of CD31 (C), and α-SMA (E). Quantification of E-cadherin (B), CD31 (D) and α-SMA expression (F) in the 4T1, 67NR and MNU-induced models. Data are mean ± SEM. *P* values were determined using Welch one-way ANOVA test and the one-way ANOVA test. Scale bars, 100 μm. E, early stage; L, late stage. [Color figure can be viewed at wileyonlinelibrary.com]

strategies for flow cytometry analyses are shown (Figure S2D-G). Mice bearing 4T1 tumors exhibited significantly higher frequencies of CD4+ and CD8+ T cells than the 67NR model (*P* < .01; *P* < .01;

Figure 4A). However, immunophenotyping did not reveal obvious differences in the subsets of NK cells, macrophages and neutrophils between the 4T1 and 67NR models.
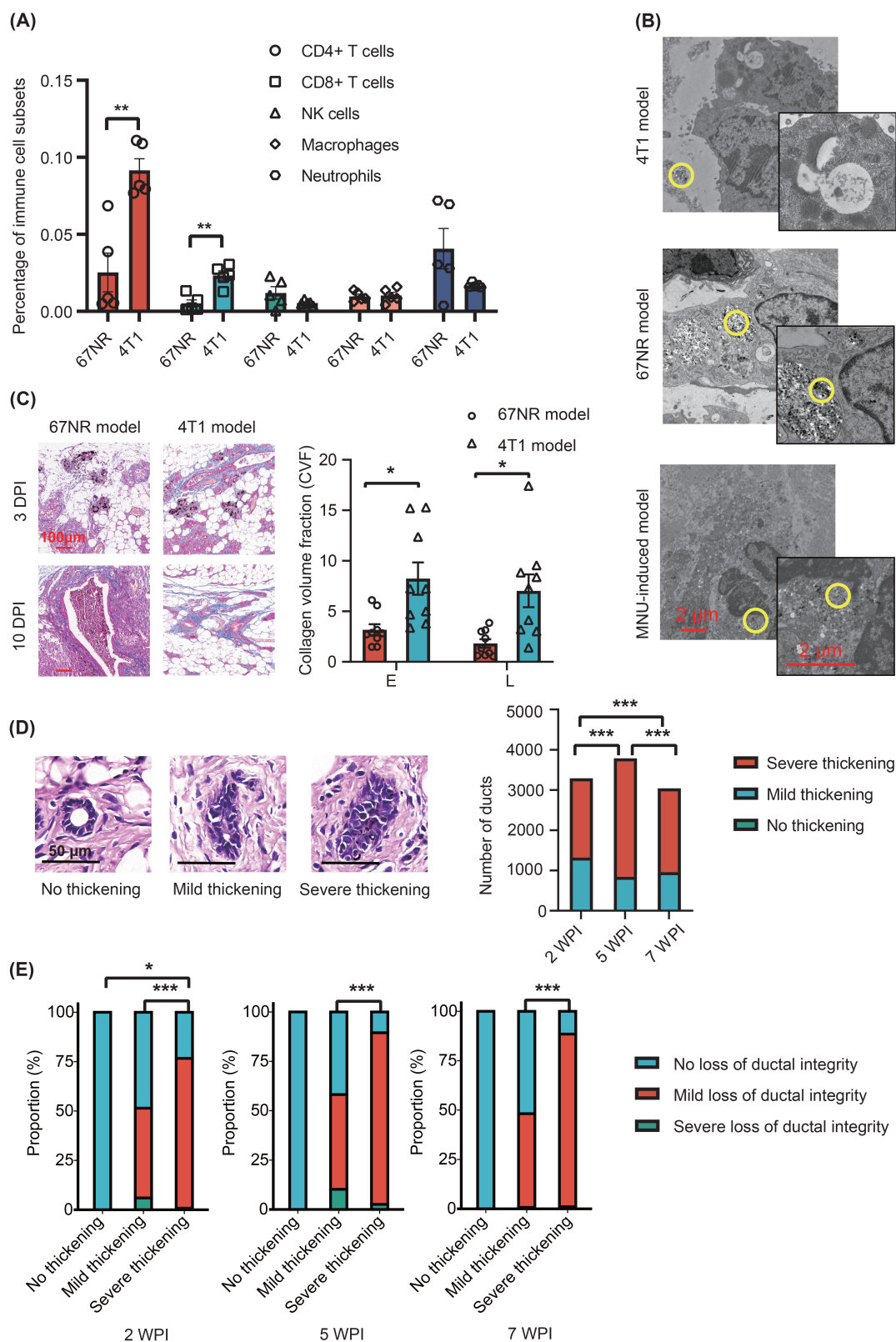
FIGURE 4 Morphological changes during tumor progression imply that ER-positive tumors gradually increased in size within the lumen before the invasion. (A) Tumor infiltration of immune cell subsets by flow cytometry. (B) The TEM images reveal the subcellular localization of CNPs (yellow circle). Scale bars, 2 μm. (C) The immunohistochemical staining and quantification of Masson's staining in the 4T1 and 67NR models. Scale bars, 100 μm. (D) The histological evaluation and statistical analysis of breast tumors regarding the ductal thickening. Scale bars, 50 μm. (E) Comparison of the ratio of ducts with a distinct loss of integrity in normal, mild thickening and severe thickening ducts between different stages. Data are mean ± SEM. Pearson's χ^2 test was used to compare proportions and evaluate the P-value. E, early stage; L, late stage. [Color figure can be viewed at wileyonlinelibrary.com]

Additionally, we observed CNPs under TEM to obtain their cellular localization. CNPs were revealed to be phagocytosed by the fibroblasts rather than the tumor cells in both the 67NR model and MNU-induced model (Figure 4B). The vimentin immunostaining revealed fibroblasts in positions where CNPs were arranged in the MNU-induced mammary tumors (Figure S1D). However, in the 4T1 model, CNPs were not found to be taken by fibroblasts or macrophages (Figure 4B).

3.4 | Morphological changes during tumor progression imply that ER-positive tumors gradually increased in size within the lumen before the invasion

The effect of the allograft modeling method on tumor invasion behavior is discussed in the third part of this study. However, the MNU-induced model used here has further advantages over allograft models such as the 4T1 and 67NR models. In the MNU-induced model by intraductal route, carcinogens induce oncogenic mutations and tumor promoters lead to the expansion of a cell population affected by the carcinogen orthotopically.[39] It suggests that chemically induced carcinogenesis is a better mimic of naturally occurring carcinogenesis. Therefore, in the allograft models, the thickness of the duct lining was no longer evaluated and a deeper understanding of invasion was not performed.

Based on the thickness of the duct lining and cellularity of the inner margins of the ducts, MNU-induced tumors were evaluated (Figure 4D). Exactly 3 (0.1%) out of 3293 ducts were classified as normal ducts, 1320 (40.1%) were classified as ducts with mild thickening, and 1970 (59.8%) were classified to be severely thickened at 2 WPI. This classification divided all ducts in the 5 WPI group into ducts with mild thickening or severe thickening. Similar conditions were found at 7 WPI. Combined with the luminal architecture analysis above, these results confirmed the increases in the thickness of the duct lining and the loss of luminal architecture over tumor progression in the rats.

Next, we investigated the relationship between these pathological features to understand the invasion of MNU-induced tumors in detail. Statistical tests revealed significant variance in the rate of different degrees of ductal integrity loss among varying thickening groups in the MNU-induced model (Figure 4E). At 2 WPI, the rate of ducts with no loss of luminal architecture in the severe thickening group was significantly less than the no thickening group ($P = .023$) and the moderate thickening group ($P < .001$). Similar results were shown at 5 WPI and 7 WPI, except for the ratio of ducts with no defects between the severe thickening group and the no thickening group. One probable reason is that there were fewer ducts with loss of integrity in the no thickening group. Overall, these results suggested that ducts with increased thickening of the breast duct lining are less likely to retain their integrity. It indicated that for MNU-induced ER-positive BC, late-stage tumors gradually increase in size and are then able to penetrate the epithelial layer.

4 | DISCUSSION

Compared to other phenotypes such as TNBC, patients with ER-positive subtype BC have a lower risk of metastatic disease.[46] The specific mechanism behind their distinct prognosis remains to be explored, especially in view of invasive behavior. To explore the invasive mode of these two subtypes, we managed to monitor the invasion behavior of BC cells by tracking the movement of nanomaterials post intraductal inoculation. We developed three intraductal BC models representing the ER-positive subtype and triple-negative subtype. Specifically, the MNU-induced model and 67NR allograft model serve as animal models for ER-positive BC, whereas the 4T1 mouse allograft model serves as the TNBC model.

This study first proved that post intraductal administration, the distribution of CNPs is able to reflect the motion of mammary cancer cells. Next, the quantification of the lesion of CNPs and tumor cells invading neighboring tissue as a proportion of the total area was evaluated. Both the area percentage of CNPs and tumor cells penetrating the epithelium of the mammary duct in late-stage tumors was found significantly higher than that in early-stage tumors in the MNU-induced model, while the TNBC model gave the opposite result. Consequently, we conjectured that the invasiveness of MNU-induced cancer cells increases with tumor progression while early triple-negative tumors exhibit high invasiveness closely analogous to that of the late tumors.

Then histological evaluation was conducted to explain the distinct invasion modes of the MNU-induced and 4T1 models. Regarding duct integrity, there were significant differences between the early tumors and the late tumors in the ER-positive phenotype. Conversely, there were no such disparities found in the TNBC mouse model. Therefore, the distinct invasive pattern between these two models could be interpreted based on these morphological differences. Furthermore, similar results were detected in these two models when comparing the distribution of CNPs within the ducts between groups with varying loss of luminal architecture. It turned out that CNPs prefer to aggregate in the broken ducts, further demonstrating that the distribution of CNPs can predict the invasion pattern of tumor cells.

The relationship between the duct thickness and the duct integrity provided a detailed characterization of the invasive pattern of ER-positive BC. The statistical analysis revealed that ducts with increased thickening of the breast duct lining are less likely to retain their integrity. This result suggested that ER-positive tumors gradually increase in size during the progression and then can penetrate the epithelial layer. Together, these results indicated that the ER-positive BC cells behave differently in different stages. This finding is consistent with the low proliferation and good prognosis of ER-positive BCs.[7-9] Our studies also demonstrated the distinct change mode between the ER-positive subtype and the TNBC regarding the retention of E-cadherin and α-SMA staining and vessel formation. However, we did not identify any difference in the MMP9 staining between different stages across all the models (Figure S2A,B). This discrepancy could be attributed to the way MMP9 promotes tumor invasion and angiogenesis. MMP9 regulates tumor migration and invasion by binding to CD44, a

known receptor for hyaluronic acid.[47-49] Previous studies revealed that the function of CD44-MMP9 complexes is increased with localized MMP activity rather than with continuously high activity.[50] Therefore, there may be no linear relationship between the invasiveness of tumor cells and MMP9 expression. Further, using flow cytometry, we found that there were significant differences in TIL subset distribution between ER-positive and TNBC grafting models, with 4T1 tumors exhibiting higher frequencies of CD4+ and CD8+ T cells. The results may be explained by a recent study on bone metastases in TNBC. Using the 4T1 model, Monteiro and Bonomo demonstrated that CD4+ T cells prepared the pre-metastasis niche for the further establishment of tumor cells, thus enhancing distant metastasis.[51] Thus, the increasing recruitment of CD4+ and CD8+ T cells in the 4T1 model may be the result of this preparation for the pre-metastasis niche. Further research, though, would be required to elucidate possible interpretations. Using the intraductal route and nanomaterials, we evaluated, perhaps for the first time, the invasion pattern of two BC subtypes in vivo and analyzed the detailed invasion mode of ER-positive BC.

The observed discrepancies could be due to different genotypic and phenotypic characteristics or intrinsic biochemical differences. Previous studies revealed that extracellular matrix (ECM) degradation and remodeling, cell-cell signaling, cell-ECM interactions and mechanical interactions could contribute to tumor progression.[52-54] In a TNBC microfluidic invasion, the pre-invaded macrophages were found to affect both the vascular endothelium and ECM, consequently altering the microenvironment favoring cancer invasion.[55] The collagen analysis in Maller's study highlighted that triple-negative tumors exhibited a higher level of fibrosis and collagen crosslinks than the ER-positive subtype.[56] Thus, the distinct pre-metastatic niche formation and collagen architectures may reflect differences in tissue histology and contribute to our findings, which will need further study. Furthermore, we failed to track the exact time and underlying mechanism that switches the local lesion to invasive carcinoma in vivo. To address this issue, there is a need to develop a novel technique or model that allows the real-time monitoring of biochemical signals and mechanical properties and replicates normal tumor progression in the immunocompetent tissue setting.

Given the role of CNPs as a tracer, we observed CNPs under TEM to obtain their cellular localization of them. CNPs in the two ER-positive models were phagocytosed by the fibroblasts rather than the tumor cells. Surprisingly, we did not observe any CNP taken by the fibroblasts or macrophages in the mouse BC model under TEM. Although it is unclear why the CNPs assembled in the ECM (Figure S2C) in the TNBC model, there may be two possible explanations. The possibility relates to the recent hypothesis by Sun et al that collagen fiber alignment in TNBC may dampen and obstruct immune infiltration.[57] The enhanced collagen fiber alignment in the triple-negative tumors may hinder the motility of fibroblasts. To confirm this possibility, Masson's staining was performed to identify collagen deposition. It turned out that denser collagen deposition was identified (Figure 4C) in the 4T1 models than in the 67NR tumors, which proves our conjecture.

Further, the data add to the evidence of a possible effect by the level of fibrosis on the differences between ER-positive and TNBC indirectly. Second, previous studies demonstrated a correlation between subtypes of BC and the density of macrophages infiltrating the tumor.[58-60] Therefore, compared to ER-positive tumors, the stroma of triple-negative tumors may harbor different densities of fibroblasts, affecting the intake of CNPs. Vimentin immunostaining also revealed low-density fibroblasts within triple-negative tumors (Figure S1D).

Last, we are aware that our research may have two disadvantages. First, part of the histologic evaluation is subjective, affecting the statistical analysis. Second, in the allograft ER-positive model, we failed to verify our conjecture about the unique invasion mode of the ER-positive model. After morphological evaluation, 67NR tumors were found to exhibit similar ductal breakthrough behavior to the 4T1 model. Through immunohistochemical assessment, we demonstrated that the changing pattern of the expression level of E-cadherin, α-SMA and CD31 for the 67NR model is consistent with the MNU-induced model rather than the 4T1 model. Considering the distinct molecular phenotyping between 67NR and 4T1 cell lines, these findings led us to surmise that the process of the allograft model affected the ductal breakthrough behavior of tumors. Therefore, the 67NR tumor cells exhibited a similar ductal breakthrough pattern as the 4T1 model. But another important perspective can be derived from our work. The common invasion behavior mode between the 4T1 and 67NR models suggested that the invasion behavior of tumor cells in allograft models is affected by the modeling method.

In conclusion, this study suggested the invasion patterns of ER-positive BC in vivo. The ER-positive BC cells prefer local colonization and proliferation and tumor cells invade and migrate until the tumor within the ducts is large enough to break through the duct lining. In contrast, triple-negative breast tumor cells exhibit strong invasiveness earlier.

AUTHOR CONTRIBUTIONS

Xinwen Kuang: Performed experiments; Performed data analysis; Drafted the article. **Zixuan Luo:** Performed experiments; Performed data analysis. **Zhihong Sun:** Performed experiments; Performed data analysis. **Jiawei Hu:** Performed experiments. **Jianhua Liu:** Performed experiments. **Deguang Kong:** Provided guidance. **Guannan Wang:** Provided guidance. **Liantao Guo:** Performed experiments. **Lan Luo:** Performed experiments. **Weijie Zheng:** Performed experiments. **Shengrong Sun:** Supervised the entire work. **Yan Rao:** Performed experiments; Supervised the entire work. **Chuang Chen:** Supervised the entire work. The work reported in the article has been performed by the authors, unless clearly specified in the text.

ACKNOWLEDGEMENTS

CONFLICT OF INTEREST STATEMENT

The authors declare no conflicts of interest.

DATA AVAILABILITY STATEMENT

The data that support the findings of this study are available from the corresponding author upon reasonable request.

ETHICS STATEMENT

The study was approved by the Laboratory Animal Welfare & Ethics Committee, Renmin Hospital of Wuhan University (under a projected license No.: 20211001).

ORCID

Xinwen Kuang https://orcid.org/0000-0002-6876-7844
Shengrong Sun https://orcid.org/0000-0003-2893-6735

REFERENCES

1. Siegel RL, Miller KD, Fuchs HE, Jemal A. Cancer statistics, 2021. *CA Cancer J Clin*. 2021;71:7-33.
2. Pommier RM, Sanlaville A, Tonon L, et al. Comprehensive characterization of claudin-low breast tumors reflects the impact of the cell-of-origin on cancer evolution. *Nat Commun*. 2020;11:3431.
3. Cancer Genome Atlas Network. Comprehensive molecular portraits of human breast tumours. *Nature*. 2012;490:61-70.
4. Perou CM, Sr T, Eisen MB, et al. Molecular portraits of human breast tumours. *Nature*. 2000;406:747-752.
5. Rakha EA, Elsheikh SE, Aleskandarany MA, et al. Triple-negative breast cancer: distinguishing between basal and nonbasal subtypes. *Clin Cancer Res*. 2009;15:2302-2310.
6. Tobin NP, Harrell JC, Lv J, et al. Molecular subtype and tumor characteristics of breast cancer metastases as assessed by gene expression significantly influence patient post-relapse survival. *Ann Oncol*. 2015; 26:81-88.
7. Cheang MC, Chia SK, Voduc D, et al. Ki67 index, HER2 status, and prognosis of patients with luminal B breast cancer. *J Natl Cancer Inst*. 2009;101:736-750.
8. Sr T, Perou CM, Tibshirani R, et al. Gene expression patterns of breast carcinomas distinguish tumor subclasses with clinical implications. *Proc Natl Acad Sci U S A*. 2001;98:10869-10874.
9. Adams S, Diamond JR, Hamilton E, et al. Atezolizumab plus nab-paclitaxel in the treatment of metastatic triple-negative breast cancer with 2-year survival follow-up: a phase 1b clinical trial. *JAMA Oncol*. 2019;5:334-342.
10. Foulkes WD, Smith IE, Reis-Filho JS. Triple-negative breast cancer. *N Engl J Med*. 2010;363:1938-1948.
11. Tai F, Gong K, Song K, He Y, Shi J. Enhanced JunD/RSK3 signalling due to loss of BRD4/FOXD3/miR-548d-3p axis determines BET inhibition resistance. *Nat Commun*. 2020;11:258.
12. Collignon J, Lousberg L, Schroeder H, Jerusalem G. Triple-negative breast cancer: treatment challenges and solutions. *Breast Cancer*. 2016;8:93-107.
13. Wang W, Nag SA, Zhang R. Targeting the NFκB signaling pathways for breast cancer prevention and therapy. *Curr Med Chem*. 2015;22: 264-289.
14. Nusse R, Clevers H. Wnt/β-catenin signaling, disease, and emerging therapeutic modalities. *Cell*. 2017;169:985-999.
15. Shen M, Jiang YZ, Wei Y, et al. Tinagl1 suppresses triple-negative breast cancer progression and metastasis by simultaneously inhibiting integrin/FAK and EGFR signaling. *Cancer Cell*. 2019;35:64-80.e7.
16. Liu Q, He L, Li S, et al. HOMER3 facilitates growth factor-mediated β-catenin tyrosine phosphorylation and activation to promote metastasis in triple negative breast cancer. *J Hematol Oncol*. 2021;14:6.
17. Méndez O, Peg V, Salvans C, et al. Extracellular HMGA1 promotes tumor invasion and metastasis in triple-negative breast cancer. *Clin Cancer Res*. 2018;24:6367-6382.
18. Hu MH, Wu TY, Huang Q, Jin G. New substituted quinoxalines inhibit triple-negative breast cancer by specifically downregulating the c-MYC transcription. *Nucleic Acids Res*. 2019;47:10529-10542.
19. Burstein MD, Tsimelzon A, Poage GM, et al. Comprehensive genomic analysis identifies novel subtypes and targets of triple-negative breast cancer. *Clin Cancer Res*. 2015;21:1688-1698.
20. Johnstone CN, Pattison AD, Harrison PF, et al. FGF13 promotes metastasis of triple-negative breast cancer. *Int J Cancer*. 2020;147: 230-243.
21. Jiang K, Liu P, Xu H, et al. SASH1 suppresses triple-negative breast cancer cell invasion through YAP-ARHGAP42-Actin axis. *Oncogene*. 2020;39:5015-5030.
22. Gagliano T, Shah K, Gargani S, et al. PIK3Cδ expression by fibroblasts promotes triple-negative breast cancer progression. *J Clin Invest*. 2020;130:3188-3204.
23. Gao D, Liu J, Yuan J, et al. Intraductal administration of N-methyl-N-nitrosourea as a novel rodent mammary tumor model. *Ann Transl Med*. 2021;9:576.
24. McCormick DL, Adamowski CB, Fiks A, Moon RC. Lifetime dose-response relationships for mammary tumor induction by a single administration of N-methyl-N-nitrosourea. *Cancer Res*. 1981;41: 1690-1694.
25. Thompson HJ, Adlakha H. Dose-responsive induction of mammary gland carcinomas by the intraperitoneal injection of 1-methyl-1-nitrosourea. *Cancer Res*. 1991;51:3411-3415.
26. Thompson HJ, McGinley JN, Rothhammer K, Singh M. Rapid induction of mammary intraductal proliferations, ductal carcinoma in situ and carcinomas by the injection of sexually immature female rats with 1-methyl-1-nitrosourea. *Carcinogenesis*. 1995;16:2407-2411.
27. Murata S, Kominsky SL, Vali M, et al. Ductal access for prevention and therapy of mammary tumors. *Cancer Res*. 2006;66:638-645.
28. Behbod F, Kittrell FS, LaMarca H, et al. An intraductal human-in-mouse transplantation model mimics the subtypes of ductal carcinoma in situ. *Breast Cancer Res*. 2009;11:R66.
29. Russell TD, Jindal S, Agunbiade S, et al. Myoepithelial cell differentiation markers in ductal carcinoma in situ progression. *Am J Pathol*. 2015;185:3076-3089.
30. Steenbrugge J, Breyne K, Denies S, et al. Comparison of the adipose and luminal mammary gland compartment as orthotopic inoculation sites in a 4T1-based immunocompetent preclinical model for triple-negative breast cancer. *J Mammary Gland Biol Neoplasia*. 2016;21: 113-122.
31. Sflomos G, Dormoy V, Metsalu T, et al. A preclinical model for ERα-positive breast cancer points to the epithelial microenvironment as determinant of luminal phenotype and hormone response. *Cancer Cell*. 2016;29:407-422.
32. Steenbrugge J, Breyne K, Demeyere K, et al. Anti-inflammatory signaling by mammary tumor cells mediates prometastatic macrophage polarization in an innovative intraductal mouse model for triple-negative breast cancer. *J Exp Clin Cancer Res*. 2018;37:191.
33. Boiy R, Steenbrugge J, Van Deun J, Hendrix A, Meyer E, De Wever O. Transparent reporting of experimental parameters in assays measuring phenotypic steps in metastasis. *Clin Exp Metastasis*. 2018; 35:715-725.

34. Atiya HI, Dvorkin-Gheva A, Hassell J, et al. Intraductal adaptation of the 4T1 mouse model of breast cancer reveals effects of the epithelial microenvironment on tumor progression and metastasis. *Anticancer Res*. 2019;39:2277-2287.

35. Liu P, Tan J, Tan Q, Xu L, He T, Lv Q. Application of carbon nanoparticles in tracing lymph nodes and locating tumors in colorectal cancer: a concise review. *Int J Nanomedicine*. 2020;15:9671-9681.

36. Tian Y, Lin Y, Guo H, et al. Safety and efficacy of carbon nanoparticle suspension injection and indocyanine green tracer-guided lymph node dissection during robotic distal gastrectomy in patients with gastric cancer. *Surg Endosc*. 2022;36:3209-3216.

37. Wang Q, Chen E, Cai Y, et al. Preoperative endoscopic localization of colorectal cancer and tracing lymph nodes by using carbon nanoparticles in laparoscopy. *World J Surg Oncol*. 2016;14:231.

38. Wang R, Mo S, Liu Q, et al. The safety and effectiveness of carbon nanoparticles suspension in tracking lymph node metastases of colorectal cancer: a prospective randomized controlled trial. *Jpn J Clin Oncol*. 2020;50:535-542.

39. Williams GM. Epigenetic effects of liver tumor promoters and implications for health effects. *Environ Health Perspect*. 1983;50:177-183.

40. Kokubun K, Matsumura S, Yudasaka M, Iijima S, Shiba K. Immobilization of a carbon nanomaterial-based localized drug-release system using a bispecific material-binding peptide. *Int J Nanomedicine*. 2018;13:1643-1652.

41. Ge W, Li Q, Liu WJ, et al. Carbon nanoparticle suspension could help get a more accurate nodal staging for patient with rectal cancer. *Sci Rep*. 2021;11:9933.

42. Lv S, Li Y, Zhang K, Lin Z, Tang D. Carbon dots/g-C(3)N(4) nanoheterostructures-based signal-generation tags for photoelectrochemical immunoassay of cancer biomarkers coupling with copper nanoclusters. *ACS Appl Mater Interfaces*. 2017;9:38336-38343.

43. Sukumar S, Notario V, Martin-Zanca D, Barbacid M. Induction of mammary carcinomas in rats by nitroso-methylurea involves malignant activation of H-ras-1 locus by single point mutations. *Nature*. 1983;306:658-661.

44. Savas P, Salgado R, Denkert C, et al. Clinical relevance of host immunity in breast cancer: from TILs to the clinic. *Nat Rev Clin Oncol*. 2016;13:228-241.

45. Miller LD, Chou JA, Black MA, et al. Immunogenic subtypes of breast cancer delineated by gene classifiers of immune responsiveness. *Cancer Immunol Res*. 2016;4:600-610.

46. Tekpli X, Lien T, Rs AH, et al. An independent poor-prognosis subtype of breast cancer defined by a distinct tumor immune microenvironment. *Nat Commun*. 2019;10:5499.

47. Gonzalez-Avila G, Sommer B, Mendoza-Posada DA, Ramos C, Garcia-Hernandez AA, Falfan-Valencia R. Matrix metalloproteinases participation in the metastatic process and their diagnostic and therapeutic applications in cancer. *Crit Rev Oncol Hematol*. 2019;137:57-83.

48. Sternlicht MD, Werb Z. How matrix metalloproteinases regulate cell behavior. *Annu Rev Cell Dev Biol*. 2001;17:463-516.

49. Egeblad M, Werb Z. New functions for the matrix metalloproteinases in cancer progression. *Nat Rev Cancer*. 2002;2:161-174.

50. Joseph C, Alsaleem M, Orah N, et al. Elevated MMP9 expression in breast cancer is a predictor of shorter patient survival. *Breast Cancer Res Treat*. 2020;182:267-282.

51. Monteiro AC, Bonomo A. Dendritic cells development into osteoclast-type APCs by 4T1 breast tumor T cells milieu boost bone consumption. *Bone*. 2021;143:115755.

52. Qian T, Liu C, Ding Y, et al. PINCH-1 interacts with myoferlin to promote breast cancer progression and metastasis. *Oncogene*. 2020;39:2069-2087.

53. Vasiukov G, Novitskaya T, Zijlstra A, et al. Myeloid cell-derived TGFβ signaling regulates ECM deposition in mammary carcinoma via adenosine-dependent mechanisms. *Cancer Res*. 2020;80:2628-2638.

54. Zhang Y, Yan WT, Yang ZY, et al. The role of WT1 in breast cancer: clinical implications, biological effects and molecular mechanism. *Int J Biol Sci*. 2020;16:1474-1480.

55. Kim H, Chung H, Kim J, et al. Macrophages-triggered sequential remodeling of endothelium-interstitial matrix to form pre-metastatic niche in microfluidic tumor microenvironment. *Adv Sci*. 2019;6:1900195.

56. Maller O, Drain AP, Barrett AS, et al. Tumour-associated macrophages drive stromal cell-dependent collagen crosslinking and stiffening to promote breast cancer aggression. *Nat Mater*. 2021;20:548-559.

57. Sun X, Wu B, Chiang HC, et al. Tumour DDR1 promotes collagen fibre alignment to instigate immune exclusion. *Nature*. 2021;599:673-678.

58. Boyle ST, Poltavets V, Kular J, et al. ROCK-mediated selective activation of PERK signalling causes fibroblast reprogramming and tumour progression through a CRELD2-dependent mechanism. *Nat Cell Biol*. 2020;22:882-895.

59. DeNardo DG, Brennan DJ, Rexhepaj E, et al. Leukocyte complexity predicts breast cancer survival and functionally regulates response to chemotherapy. *Cancer Discov*. 2011;1:54-67.

60. Acerbi I, Cassereau L, Dean I, et al. Human breast cancer invasion and aggression correlates with ECM stiffening and immune cell infiltration. *Integr Biol*. 2015;7:1120-1134.

SUPPORTING INFORMATION

Additional supporting information can be found online in the Supporting Information section at the end of this article.